Chinese Chemical Letters 33 (2022) 3065–3072

Contents lists available at ScienceDirect

Chinese Chemical Letters

journal homepage: www.elsevier.com/locate/cclet

Promotional effect of Cu additive for the selective catalytic oxidation of *n*-butylamine over $CeZrO_x$ catalyst

Xin Xing[a,b], Ting Zhao[a], Jie Cheng[a,*], Xiaoxiao Duan[a], Wenpeng Li[a], Ganggang Li[a], Zhongshen Zhang[a], Zhengping Hao[a]

[a] *National Engineering Laboratory for VOCs Pollution Control Material & Technology, Research Center for Environmental Material and Pollution Control Technology, University of Chinese Academy of Sciences, Beijing 101408, China*

[b] *College of Environmental Science and Engineering, Taiyuan University of Science and Technology, Taiyuan 030024, China*

ARTICLE INFO

Article history:
Received 26 July 2021
Revised 20 August 2021
Accepted 16 September 2021
Available online 23 September 2021

Keywords:
N-Butylamine
$CeCu_aZrO_x$ mixed oxide
Selective oxidation
Oxygen vacancies
Reaction mechanism

ABSTRACT

The catalytic elimination of nitrogen-containing volatile organic compounds (NVOCs) still encounters bottlenecks in NO_x formation and low N_2 selectivity. Here, a series of Cu-promoted Ce-Zr mixed oxide catalysts were synthesized using a simple precipitation approach, and *n*-butylamine was adopted as the probe pollutant to evaluate their catalytic performance. The $CeCu_{10\%}ZrO_x$ catalyst exhibited the best catalytic activity, with 100% *n*-butylamine conversion and 90% N_2 selectivity at 250 °C. Concurrently, this sample also displayed good water resistance. A detailed characterization of the catalyst was performed through a series of experimental studies and theoretical calculations. The addition of Cu increased the redox property and promoted the production of oxygen vacancies, all of which were favorable for the greatest *n*-butylamine selective catalytic oxidation performance. The changes of oxygen vacancies over $CeCu_{10\%}ZrO_x$ in reaction process were studied by *in situ* Raman spectra. Moreover, *in situ* diffuse reflectance infrared Fourier transform spectra (DRIFTs) and theoretical calculations were employed to explore the reaction mechanism of *n*-butylamine selective oxidation. The high activity and selectivity of this catalyst confirm the practical feasibility of the selective oxidation of *n*-butylamine to CO_2 and N_2, and the exploration of the reaction mechanism provides new insights into the further design of catalysts.

Main volatile organic compounds (VOCs) are crucial precursors of secondary organic aerosol, ozone pollution, and photochemical smog [1–5]. Nitrogen-containing VOCs (NVOCs), such as acrylonitrile, *n*-butylamine and *N,N*-dimethylformamide, which are typical NVOCs, are most frequently in the emission of the petrochemical, pharmaceutical, coating industries [3,6]. NVOCs will cause substantial pollution to the environment and exert strong toxic effects on the human body. For the elimination of NVOCs, the traditional combustion technology usually operates at high temperatures, which leads to highly energy consumption and secondary pollutant NO_x formation [7]. Conversely, selective catalytic oxidation (SCO) technology can realize selective generation of nitrogen and reduce the generation of nitrogen oxides [8]. Therefore, effective catalysts with a high catalytic conversion rate and N_2 selectivity in the decomposition of NVOCs must be explored.

A number of studies describing the catalytic degradation of NVOCs have been published. According to Nanba *et al.*, Cu/ZSM-5 could completely convert acrylonitrile with an N_2 selectivity of at least 80% at a temperature greater than 350 °C [7-9]. Zhang *et al.* reported the nearly complete conversion of acetonitrile by Cu/SBA-15 that was associated with an N_2 selectivity of approximately 80% at $T > 300$ °C, and thus Cu/SBA-15 was the most promising catalyst [10]. Zhou *et al.* investigated CrCe supporting on different pillared interlayered clays catalysts for the NVOCs (*n*-butylamine, ethylenediamine, and acetonitrile) oxidation [11]. Ma *et al.* discussed the high catalytic activity of Pd-confined materials, showed the complete conversion of *n*-butylamine at 280 °C and explored the structure activity relationship and the reaction mechanism [12]. However, it is rarely reported that low temperature (< 300 °C) catalytic oxidation of NVOCs can be achieved on non-noble metal catalysts. In particular, the catalysts simultaneously exhibit high conversion and N_2 selectivity at low temperatures.

In recent years, as a rare earth metal oxide, CeO_2 has excellent oxygen storage performance, which was used to catalyze various reactions, such as nitric oxide reduction, carbon monoxide oxidation and NH_3 oxidation reactions [13–15]. Wang *et al.* observed that the CuO-CeO_2 sample exhibited highly dispersed CuO species,

---

[*] Corresponding author.
E-mail address: jiecheng@ucas.ac.cn (J. Cheng).

https://doi.org/10.1016/j.cclet.2021.09.056
1001-8417/

which possessed the highest activity in NH_3 oxidation [16]. The Ce-Zr mixed oxide has been used as a catalyst or support for NO_x selective catalytic reduction, because it combines the advantages of CeO_2 and ZrO_2. Si *et al.* impregnated CeO_2-ZrO_2 with nickel and sulfate were to improve the catalytic performance for removal of NO with NH_3 [17].

To take full advantage of the Ce-Zr mixed oxide and the promoting effect of Cu, $CeZrO_x$ and $CeCu_aZrO_x$ (a = 1%, 5%, 10%, and 15%) were synthesized using a precipitation method and tested for selective oxidation of *n*-butylamine in the present study. The catalysts showed high *n*-butylamine conversion rates and N_2 selectivity. Moreover, the structure, physical properties, oxygen species, and redox ability of catalysts were also characterized by various techniques, and the reaction mechanism underlying the catalytic degradation of *n*-butylamine was also discussed.

The structure and physical properties of $CeCu_aZrO_x$ catalysts were characterized by X-ray diffraction (XRD), high resolution transmission electron microscopy (HR-TEM) and N_2 adsorption/desorption. The XRD results of $CeCu_aZrO_x$ catalysts are shown in Fig. S1 (Supporting information). $CeZrO_x$ displayed four main peaks at approximately 29.1°, 33.7°, 48.5° and 57.5°, consistent with the structure of $Ce_{0.6}Zr_{0.4}O_2$ (JCPDS No. 38-1439) and corresponding to the (111), (200), (220) and (311) planes. For $CeCu_aZrO_x$ catalysts, characteristic diffraction peaks for the $Ce_{0.6}Zr_{0.4}O_2$ and the ZrO_2 phase (JCPDS No. 49-1642) were obtained, indicating the weak interaction between Ce and Zr, which resulted in the segregation of CeO_2 and ZrO_2 [18,19]. For $CeCu_aZrO_x$ samples, the intensity of peaks assigned to $Ce_{0.6}Zr_{0.4}O_2$ and ZrO_2 decreased significantly as Cu content increased. No obviously characteristic diffraction peaks of Cu species were presented in XRD results, indicating that Cu species were highly dispersed on the catalyst's surface. Additionally, the CeO_2 crystallite sizes were calculated using the Scherrer equation and shown in Table S1 (Supporting information), it decreased a little as the increasing of Cu content.

HR-TEM images of $CeCu_{10\%}ZrO_x$ are shown in Figs. S2a and b (Supporting information), the lattice spacing values of 0.269, 0.291 and 0.312 nm, which were attributed to the exposed $Ce_{0.6}Zr_{0.4}O_2$ (200), ZrO_2 (111) and (111) facets of $Ce_{0.6}Zr_{0.4}O_2$, respectively. The exposure of ZrO_2 (111) facets indicated the presence of phase separation in the $CeCu_{10\%}ZrO_x$ catalyst, consistent with the XRD result. Elemental mapping was performed by energy-dispersive X-ray spectroscopy (EDX) to confirm the elemental distributions of Ce, Cu, Zr, and O species in $CeCu_{10\%}ZrO_x$. As shown in Figs. S2d-h (Supporting information), the O, Ce, Cu, and Zr species were homogeneously dispersed throughout $CeCu_{10\%}ZrO_x$, verifying that Cu^{2+} was successfully incorporated into $CeZrO_x$.

N_2 adsorption/desorption isotherms and pore size distribution of $CeCu_aZrO_x$ catalysts are shown in Fig. S3 (Supporting information). According to International Union of Pure and Applied Chemistry (IUPAC) classification, all the catalysts presented type IV isotherm curves, indicated that the samples are typical mesoporous materials. The special surface area (SSA), pore volume and pore size are calculated by N_2 physical adsorption results of $CeZrO_x$ and $CeCu_aZrO_x$ catalysts and shown in Table S1. The addition of CuO in $CeZrO_x$ had a significant impact on the special surface area. As the contents of Cu increased from 1% to 15%, the SSA of the samples grew from 61 to 85 m^2/g, $CeCu_{15\%}ZrO_x$ exhibited the largest surface area of 85 m^2/g. The results showed that the introduction of Cu into the $CeZrO_x$ could lead to the change of the structure, further result in the higher specific surface area [20], which is instrumental in the dispersion of Cu species.

The conversion of *n*-butylamine and characteristic activity data are shown in Fig. 1a and Table S1. Obviously, the addition of Cu increased the *n*-butylamine conversion in all samples. The temperature recorded at 50% and 90% *n*-butylamine conversion (T_{50} and T_{90}) decreased in the order $CeZrO_x > CeCu_{15\%}ZrO_x > CeCu_{10\%}ZrO_x > CeCu_{5\%}ZrO_x > CeCu_{1\%}ZrO_x$. Interestingly, the values of T_{100} decreased in the order $CeZrO_x > CeCu_{1\%}ZrO_x = CeCu_{5\%}ZrO_x > CeCu_{10\%}ZrO_x = CeCu_{15\%}ZrO_x$. The activities of $CeCuZrO_x$ catalysts were higher than the values reported in the literature (Table S2 in Supporting information). As shown in Fig. 1a, the conversion *vs.* temperature plot of *n*-butylamine oxidation over $CeZrO_x$ exhibited a relativity lower conversion rate, while complete conversion was achieved at approximately 350 °C. Furthermore, *n*-butylamine oxidation activity in the presence of Cu in $CeZrO_x$ was very similar, the conversion of *n*-butylamine progressively increased with the temperature rising, and a 100% *n*-butylamine conversion rate was achieved at about 300 °C. The *n*-butylamine conversion over $CeCu_aZrO_x$ samples is tightly related to the Cu contents. $CeCu_{10\%}ZrO_x$ and $CeCu_{15\%}ZrO_x$ exhibited the highest activity and achieved 100% *n*-butylamine conversion at 250 °C.

The selectivity to CO_2 and CO over $CeCu_aZrO_x$ catalysts during *n*-butylamine oxidation is shown in Figs. 1b and c. For CO_2 formation, as shown in Fig. 1b, the selectivity to CO_2 over $CeZrO_x$ and $CeCu_aZrO_x$ catalysts increased with the increasing of temperature and achieved 100% at a higher temperature. The shape of CO_2 selectivity showed the same trend as that of *n*-butylamine conversion rates over $CeCu_aZrO_x$, and the CO_2 selectivity increased with the increase of copper contents. For CO formation, as shown in Fig. 1c, the CO selectivity over $CeZrO_x$ and $CeCu_aZrO_x$ catalysts first increased and then decreased. Relative higher amount of CO was formed over $CeZrO_x$, and the formation of CO over $CeCu_aZrO_x$ decreased with the increase of copper contents. Above all, CO was almost not produced over $CeCu_{10\%}ZrO_x$ and $CeCu_{15\%}ZrO_x$ samples at 100–400 °C.

Figs. 1d–h present the selectivity of N-containing products (N_2, N_2O, NO, NO_2 and NH_3) of *n*-butylamine catalytic degradation over $CeCu_aZrO_x$. As seen from Fig. 1d, $CeZrO_x$ exhibited very low N_2 selectivity at temperatures ranging from 100 °C to 300 °C. The N_2 selectivity over $CeCu_aZrO_x$ catalysts first increased and then decreased with the temperature rising. And the N_2 selectivity of $CeCu_{10\%}ZrO_x$ was apparently higher than other catalysts, increased with the reaction temperature and reached a maximum of 90% at 250 °C. The increase in N_2 selectivity observed at $T < 300$ °C for $CeCu_aZrO_x$ was probably because of copper doping. The incorporation of Cu in $CeZrO_x$ might favor the generation of N_2. While at high temperatures from 300 °C to 400 °C, the decrease in N_2 selectivity was caused by the formation of NO_x. For the degradation of NVOCs, the crucial point for NVOCs catalytic oxidation lies in the enhancement of the nitrogen generation and control of NO_x production, avoiding secondary pollution.

To get an intensive study into the catalytic behaviors of $CeCu_aZrO_x$ catalysts, the undesirable byproducts (N_2O, NO, NH_3, NO_2) selectivity are respectively depicted in Figs. 1e–h. As noted, NO was the main N-containing byproducts for $CeZrO_x$ and $CeCu_aZrO_x$ catalysts. NO selectivity first increased to 8% and then decreased at $T < 250$ °C. Besides, selectivity to NO over $CeCu_aZrO_x$ increased with the raising of copper content at $T > 250$ °C. The selectivity to NO over catalysts increased upon the rising temperature and achieved 50% at 400 °C. Additionally, NO_2 was generated over $CeCu_aZrO_x$ at 300 °C, and the production of NO and NO_2 at high temperatures is the major cause for the decrease of N_2 selectivity. Fig. 1i shows N-containing product selectivity at T_{100}. $CeCu_{10\%}ZrO_x$ had the highest N_2 selectivity, as well as the lowest NO selectivity. Less NH_3 formation occurred with $CeCu_{5\%}ZrO_x$, $CeCu_{10\%}ZrO_x$ and $CeCu_{15\%}ZrO_x$ than with $CeCu_{1\%}ZrO_x$ and $CeZrO_x$. N_2 was the main product generated by $CeCu_{10\%}ZrO_x$, and thus this catalyst represents a promising candidate for *n*-butylamine selective catalytic oxidation. At temperatures greater than T_{100}, the nitrogen balance was more than 95% for $CeCu_aZrO_x$ catalysts.

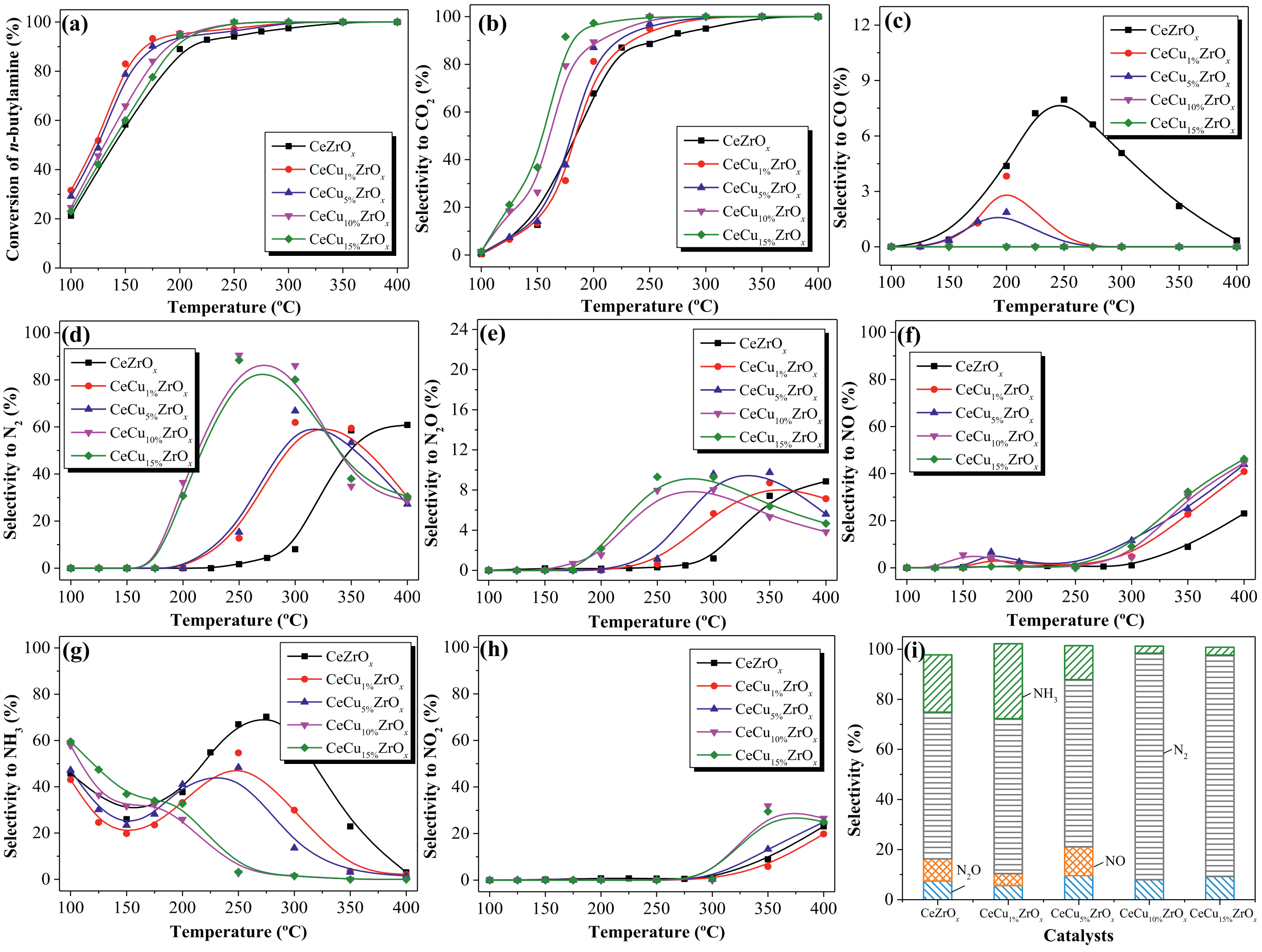

Fig. 1. Effect of temperature on (a) conversion of *n*-butylamine, (b) CO_2 selectivity and (c) CO selectivity. (d) N_2 selectivity, (e) N_2O selectivity, (f) NO selectivity, (g) NH_3 selectivity, (h) NO_2 selectivity, and (i) product selectivity in *n*-butylamine oxidation at T_{100} for $CeCu_aZrO_x$ catalysts.

The catalytic degradation of exhaust containing water vapor may result in the deactivation of catalysts in practical application. Hence, the investigation of the effect of H_2O on the catalytic performance of $CeCu_{10\%}ZrO_x$ is worthwhile. As shown in Fig. S4 (Supporting information), the addition of 15 vol% H_2O exerted little inhibition effect on *n*-butylamine conversion. A 100% *n*-butylamine conversion rate was obtained at $T > 250$ °C, which was the same as that of the reaction without H_2O. Moreover, N_2 selectivity was slightly decreased to 85% by the addition of H_2O. The decrease in N_2 selectivity in the reaction with $CeCu_{10\%}ZrO_x$ was accompanied by increases in NH_3 and NO_x formation. H_2O exists in the reaction atmosphere as a reactant, and there is competitive adsorption with reactant molecules *n*-butylamine and oxygen, resulting in the decrease of N_2 selectivity and the formation of other nitrogen-containing products. The formation of NH_3 may be due to the presence of H_2O. H_2O molecule will participate in the reaction after decomposition, and $^*NH_2$ species are more likely to produce NH_3. Briefly, the $CeCu_{10\%}ZrO_x$ catalyst exhibited good resistance to H_2O and thus it is potentially useful for eliminating *n*-butylamine from the exhaust containing a certain amount of H_2O.

The capability of oxygen species transmission and migration on Ce-Zr based catalysts are vital factors in catalytic oxidation reactions, which were evaluated using O_2 temperature-programmed desorption (O_2-TPD), UV-vis diffuse reflectance spectra (UV-vis DRs), X-ray photoelectron spectra (XPS) and Raman. The O_2-TPD patterns of the $CeCu_aZrO_x$ samples are presented in Fig. S5 (Supporting information) and could be divided into three areas. The desorption peak centered at $T < 200$ °C, is characteristic of the desorption of ordinarily chemically adsorbed oxygen species. The area at the temperature range of 200-600 °C is ascribed to the desorption of oxygen chemically adsorbed on the oxygen vacancies [21]. And the third area appeared at high temperatures, which could be attributed to the bulk lattice oxygen [22]. The lattice oxygen of $CeZrO_x$ and $CeCu_{1\%}ZrO_x$ catalysts did not appear in this temperature range, indicating that the desorption of lattice oxygen species in these samples required a higher temperature. The desorption temperatures of the first peaks decreased in the order that: $CeZrO_x > CeCu_{15\%}ZrO_x > CeCu_{10\%}ZrO_x > CeCu_{5\%}ZrO_x > CeCu_{1\%}ZrO_x$, which was related to the catalytic activity of *n*-butylamine at lower temperatures (T_{50} and T_{90}). It indicating that chemisorbed oxygen species was more conducive to the low-temperature activation of pollutant molecules and further oxidation to produce CO_2 and H_2O.

The electronic states of $CeCu_aZrO_x$ catalysts were obtained from UV-vis-DRs and shown in Fig. S6 (Supporting information). The band at *ca.* 218 nm could be assigned to tetravalent Zr species with eight-coordinated [23]. The band near 245 nm corresponded to the charge transfer transitions between O^{2-} and Ce^{3+}, which indicated the existence of oxygen vacancy. The bands for all catalysts around

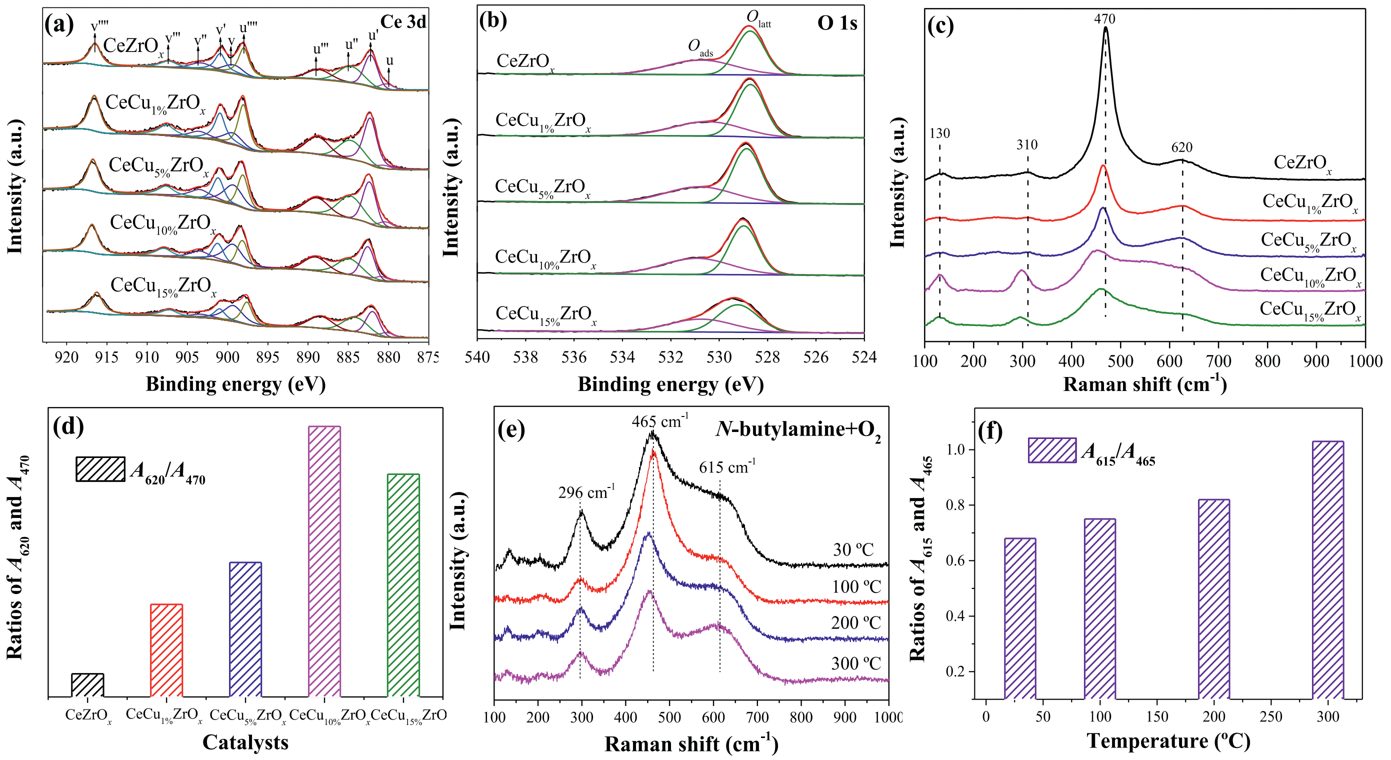

Fig. 2. X-ray photoelectron spectra for (a) Ce 3d, (b) O 1s of CeCu$_a$ZrO$_x$ catalysts. Raman spectra (c) and the concentration of surface oxygen vacancies (d) of CeCu$_a$ZrO$_x$ catalysts. *In situ* visible Raman spectra (e) and A_{615}/A_{465} (f) of CeCu$_{10\%}$ZrO$_x$.

310 nm and 341 nm were attributed to the charge transfer and inter band transitions of $O^{2-}$and Ce^{4+}, respectively [24,25]. Based on these results, both Ce^{3+} and Ce^{4+} species were present in these samples, consistent with the XPS results.

The surface chemical state of CeCu$_a$ZrO$_x$ catalysts was obtained from an XPS analysis, and the results are presented in Fig. 2. The surface compositions of the samples (Cu, Ce, Zr and O) are displayed in Table S3 (Supporting information). The XPS results for the Ce3d spectra of CeZrO$_x$ and CeCu$_a$ZrO$_x$ catalysts are shown in Fig. 2a. The labels are used to identify Ce 3d peaks, where u and v refer to the 3d$_{3/2}$ and 3d$_{5/2}$ spin-obit components, respectively. The peaks referred to as u, u′′, v, and v′′ were assigned to Ce^{3+} species and the other six peaks (u′, u′′′, u′′′′, v′, v′′′ and v′′′′) represented the presence of Ce^{4+} [26]. Thus, Ce was in a partially reduced state on the surfaces of the catalysts, which might be ascribed to the interaction between Cu and Ce. Moreover, the presence of Ce^{3+} led to a charge imbalance that was assigned to the formation of oxygen vacancies, consistent with the charge compensation. The surface Ce^{3+} concentration of total Ce (Ce^{3+} + Ce^{4+}) on the CeCu$_{10\%}$ZrO$_x$ was 0.40 (Table S3), which was higher than other samples and indicted the formation of more oxygen vacancies on CeCu$_{10\%}$ZrO$_x$. The high Ce^{3+} content in CeCu$_{10\%}$ZrO$_x$ might result from the increased reducibility of CeO_2 caused by the synergistic effect of Cu species and Ce species. As shown in Table S3, the incorporation of Cu into these samples significantly increases the proportion of $Ce^{3+}/(Ce^{3+} + Ce^{4+})$. We believe that is due to the Cu species introduction and the transfer of electrons from Cu^{+} to Ce^{4+}.

Fig. 2b displays the O 1s XPS spectra for CeCu$_a$ZrO$_x$ catalysts. The main peak was observed at around 529.4 eV and assigned to the lattice oxygen of catalysts. And the shoulder peak centered at 531.5 eV could be ascribed to the chemisorbed oxygen species [27]. According to the literature, in the oxidation reaction, the surface chemisorbed oxygen is more active than lattice oxygen because of its strong mobility [28]. Moreover, the percentages of O_{ads}/O_{latt} are calculated and shown in Table S3 (Supporting information). Compared with CeZrO$_x$, higher contents of chemisorbed oxygen were observed on the surface of CeCu$_a$ZrO$_x$, implying that Cu introduction increased the concentration of activated adsorbed oxygen species. Additionally, the percentages of O_{ads} and O_{latt} in CeCu$_{10\%}$ZrO$_x$ (0.79) were relatively higher among all samples, suggesting that more chemisorbed oxygen species were presented on the surface of CeCu$_{10\%}$ZrO$_x$. Hence, these results indicated well catalytic activity and N_2 selectivity for the degradation of *n*-butylamine over CeCu$_{10\%}$ZrO$_x$.

The comparison of Raman spectra of CeZrO$_x$ and CeCu$_a$ZrO$_x$ catalysts is shown in Fig. 2c. Raman spectra of all samples displayed an absorption band at around 470 cm^{-1}, corresponding to the characteristic F_{2g} vibration mode of fluorite CeO_2. The broad bands at 620 cm^{-1} were assigned to oxygen vacancies and ascribed to the presence of defective structures in CeCu$_a$ZrO$_x$ samples. In addition, this finding also indicated the formation of Cu-Ce-Zr solid solution, which could enhance the formation of oxygen vacancies [29]. The weak band at 310 cm^{-1} was ascribed to the substitution of oxygen atoms from the ideal lattice positions. Finally, a weak intensity Raman peak was observed at 130 cm^{-1} and ascribed to Zr doping into the lattice of Ce, which led to the distortion of the framework symmetry. The intensity of the band at 470 cm^{-1} decreased as the copper content increased and might be related to the optical absorption of copper [30]. In addition, the existence of Cu influenced the position and intensity of the F_{2g} band at 470 cm^{-1}. Copper incorporation into CeZrO$_x$ led to a red shift (from 470 cm^{-1} to 450 cm^{-1}) and the broadening of F_{2g} peaks, which was related to the formation of oxygen vacancies. Meanwhile, the band at 620 cm^{-1} showed increasing intensity, further verifying the existence of oxygen vacancies caused by the incorporation of copper into the lattice [31]. The areas ratio of the peaks at 470 cm^{-1} (A_{470}) and 620 cm^{-1} (A_{620}) reflects the concentration of oxygen vacancies [29]. The A_{620}/A_{470} value for CeCu$_a$ZrO$_x$ rapidly increased compared with CeZrO$_x$ (Fig. 2d), suggesting that the addition of Cu resulted in a higher oxygen vacancy concentration in CeCu$_a$ZrO$_x$ samples, and we reached a similar conclusion from the theoretical calculations. Thus, the CeCu$_{10\%}$ZrO$_x$ catalyst could generate more oxygen vacancies among other samples, because of the value of A_{620}/A_{470} and the shift of the F_{2g} peaks. Finally, this catalyst would promote the performance of *n*-butylamine selective oxidation.

In situ visible Raman spectra of CeCu$_{10\%}$ZrO$_x$ catalyst under a flow of *n*-butylamine and O_2 are shown in Fig. 2e. As shown in the spectra, the main peak at around 465 cm^{-1} (F_{2g}) always dominated throughout the reaction, indicating that the catalysts maintained the major fluorite-like structure [32]. The position of the F_{2g} peak was slightly shifted toward a lower Raman peak as the reaction temperature increased from 30 °C to 300 °C, due to the thermal expansion and phonon confinement. In some studies, the downward shift of F_{2g} possibly corresponds to the thermal-induced loss of lattice O that results in the sintering of CeO_2 crystals [33]. Additionally, in some cases, the shift was also in consequence of the lattice expansion and mode softening that occurred when oxygen vacancies are created [34]. The peak at 615 cm^{-1} was attributed to the intrinsic oxygen vacancies in CeCu$_{10\%}$ZrO$_x$, which were caused by the escape of interstitial oxygen from the lattice, thus leaving oxygen vacancies in original sites [33,35]. As shown in Fig. 2f, the ratios of A_{615}/A_{465} enhanced with the increase of temperature, indicating that more oxygen vacancies were generated in the bulk phase of CeCu$_{10\%}$ZrO$_x$ due to the temperature-induced structural changes [33], and the increase in the number of oxygen vacancies promote *n*-butylamine oxidation.

Brief summary, the better catalytic performance of CeCu$_{10\%}$ZrO$_x$ depended on the formation of surface oxygen vacancies and chemisorbed oxygen species. Mixed valences of Ce^{3+} and Ce^{4+} were present in the CeCu$_a$ZrO$_x$ catalyst and accompanied the generation of oxygen vacancies due to Cu introduction. The surface Ce^{3+} concentration on CeCu$_{10\%}$ZrO$_x$ was higher than in other samples, indicating the formation of a greater number of oxygen vacancies, and the higher A_{620}/A_{470} ratio further confirmed the higher oxygen vacancy concentration of CeCu$_{10\%}$ZrO$_x$. Furthermore, the O_{ads}/O_{latt} ratio in CeCu$_{10\%}$ZrO$_x$ was higher than in all other samples, suggesting that more chemisorbed oxygen species were presented on the surface of CeCu$_{10\%}$ZrO$_x$. Hence, this catalyst displayed better performance in the catalytic oxidation of *n*-butylamine.

The chemical state of Cu species was investigated by UV-vis-DRs (Fig. S6). The CeCu$_a$ZrO$_x$ catalysts showed a weak band at around 450 nm, which could be assigned to a charge transfer band in $Cu^{2+}\rightarrow O^{2-}\rightarrow Cu^{2+}$ [36]. In addition, the CeCu$_a$ZrO$_x$ catalysts also exhibited broad bands at around 700 nm, it corresponded to the d-d transitions of Cu^{2+} in octahedral symmetry. This band shifted from 650 nm to 750 nm, indicated that the coordination environment of copper species was influenced by the Cu content [37]. Furthermore, this band shifted to a longer wavelength as Cu content increased from 1 wt% to 15 wt%, which was attributed to less CuO dispersion. Cu 2p XPS spectra for CeCu$_a$ZrO$_x$ catalysts are presented in Fig. S7 (Supporting information). Two peaks centered at 932.2 and 952.1 eV were observed and potentially attributed to Cu $2p_{3/2}$ and $2p_{1/2}$ of Cu^+, respectively, whereas two other peaks at 933.6 and 953.6 eV corresponded to the existence of Cu^{2+} [38,39]. Meanwhile, the shake-up satellite feature centered at binding energies of around 942 and 962 eV was also observed. Both Cu^+ and Cu^{2+} symmetrical peaks could be found in CeCu$_a$ZrO$_x$ catalysts. Moreover, the peak area of Cu^{2+} species was larger than that of Cu^+, indicating that the characteristics Cu species predominantly present on the surface is Cu^{2+}.

H_2-TPR measurements were performed to investigate the reduction behavior of the CeCu$_a$ZrO$_x$ catalysts, and the results are presented in Fig. S8 (Supporting information). The reduction profile of CeZrO$_x$ revealed a weak reduction peak that started at approximately 450 °C and was centered at 600 °C. This peak potentially corresponded to the reduction of Ce^{4+} to Ce^{3+}, because the reduction of Zr^{4+} occurred at a temperature greater than 1000 °C [40,41]. Additionally, the presence of a single peak for CeZrO$_x$ suggested that the reduction of surface and bulk CeO_2 occurred concurrently because of the good oxygen mobility.

Obviously, the reduction behavior of CeZrO$_x$ catalyst was altered by copper-doping. The peak at 600 °C disappeared, potentially because the reduction peak of CeO_2 shifted to low temperatures, which was promoted by Cu doping. The peak splitting of the H_2-TPR data was performed and presented in Fig. S8b (Supporting information). The profiles of samples consisted of three peaks, which were denoted as α, β and γ. According to the literature [32,42], the attributions of the peaks are listed below. The first peak (α) is ascribed to the reduction of highly dispersed CuO species, including isolated Cu^{2+} ions, and the small dimension of the Cu-O-Cu clusters. The second peak (β) is assigned to the presence of large CuO clusters. The third peak (γ) is attributed to the presence of bulk-like CuO, as well as Cu^+ and Ce^{4+} reduction [32]. Furthermore, values for H_2 consumption are present in Table S4 (Supporting information). For the CeCu$_{10\%}$ZrO$_x$ catalyst, the H_2 consumption of peak α was 0.71 mmol/g, which was the highest value observed among the samples and proved the best redox property.

Based on the analyses described above and combined with the catalytic activity data, the superior catalytic performance of CeCu$_{10\%}$ZrO$_x$ compared with CeCu$_a$ZrO$_x$ catalysts could be related to the fact that CeCu$_{10\%}$ZrO$_x$ displayed the highest redox ability, due to the presence of the reduction peak of highly dispersed copper oxide species at a lower temperature and the highest H_2 consumption of this peak among all the samples.

To identify surface intermediate species, we carried out *in situ* DRIFTs under *n*-butylamine and the condition of *n*-butylamine and O_2. Fig. 3a shows *in situ* DRIFTs during exposure of CeCu$_{10\%}$ZrO$_x$ to gas mixture containing *n*-butylamine with helium as the balance gas at room temperature. The absorption bands of *n*-butylamine were observed at 3223, 3125, 2962-2855, 1643, 1588, 1466, 1378, 1173, 1094 and 1071 cm^{-1}. The bands at 3223 and 3125 cm^{-1} were ascribed to the amino group of *n*-butylamine, the vibrations of ν(sym)NH_2 and $2\delta NH_2$, respectively. The band at 1587 cm^{-1} was also attributed to the vibration of δNH_2, and the band observed at 1094 and 1072 cm^{-1} were assigned to the vibration of ν(CN) and t(CH_2(N)) [43]. The bands centered at 2963–2855, 1466 and 1378 cm^{-1} were assigned to asymmetric and symmetric bending vibrations of the C–H bonds (ν(as)CH_3, ν(as)CH_2, ν(s)CH_3, ν(s)CH_2(N), δ(as)CH_3, δ(s)CH_3, respectively). Simultaneously, the band at 1173 cm^{-1} was also detected and attributed to the vibration of ν(C-C). The band observed at 1643 cm^{-1} corresponded to the molecular adsorption of H_2O. The DRIFT spectra of CeCu$_{10\%}$ZrO$_x$ with an exposure to 375 ppm *n*-butylamine and 5% O_2 at room temperature are shown in Fig. 3b, it was found that adding the gaseous O_2 would not change the adsorption species over CeCu$_{10\%}$ZrO$_x$.

The catalysts were exposed to reaction conditions (375 ppm *n*-butylamine and 5% O_2, with helium as the balance gas) to further ascertain the intermediate species of the reaction between *n*-butylamine and O_2. Fig. 3c illustrates *in situ* DRIFT spectra of the CeCu$_{10\%}$ZrO$_x$ catalyst in a flow of *n*-butylamine+O_2 at various temperatures. The band intensities of the adsorption spectra of *n*-butylamine decreased gradually as the temperature increased. While these band intensities decreased, the band intensity of –NH_2 (1583 cm^{-1}) increased from 100 °C to 250 °C. Additionally, some new bands appeared at a temperature above 100 °C. The bands at 2177 and 2126 cm^{-1} could be assigned to adsorbed N_2O [44].

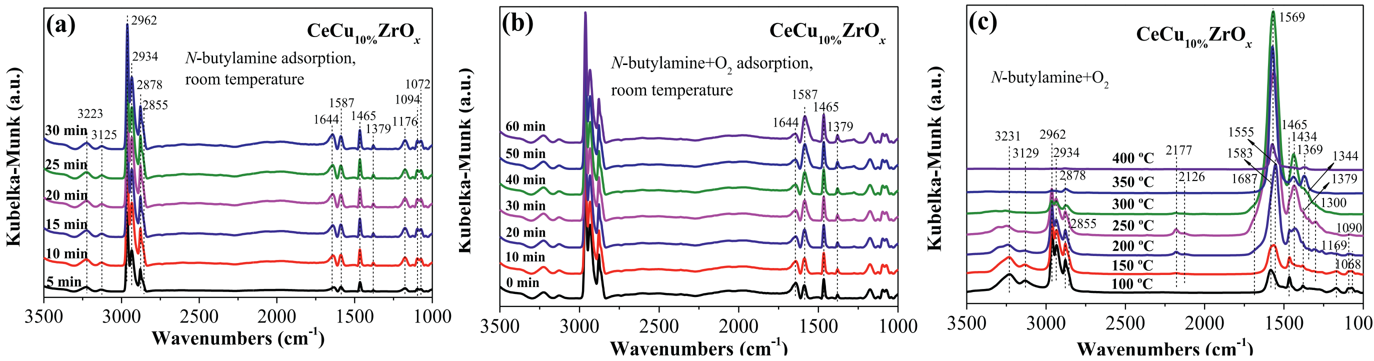

Fig 3. *In situ* DRIFTs under *n*-butylamine and the condition of *n*-butylamine + O_2.

The bands were observed at temperatures ranging from 150 °C to 300 °C, but disappeared at temperatures above 300 °C. The bands at 1555 and 1569 cm^{-1} were also detected and attributed to monodentate nitrate species and bidentate nitrate species, respectively [19,45]. Meanwhile, ionic nitrate (1369 cm^{-1}) formed. Furthermore, the existence of a peak at 1434 cm^{-1} indicated the formation of acetate species [46]. Notably, the acetate species was detected at 200 °C, and its quantity increased as the temperature increased up to 300 °C. A weak band at 1344 cm^{-1} appeared at 150 °C was attributed to the chelation of bidentate carbonate [47]. An NH_3 species was observed at 1300 cm^{-1}, and the band intensity increased monotonously as the temperature increased, but suddenly decreased at 300 °C [48].

Combining the results of DRIFT spectra and the distribution of products (Fig. 1), we were able to predict two period procedures in reaction from the formation of N_2O, N_2, NO, NO_2 and NH_3.

The following main reaction routes were proposed Eqs. 1 and 2:

$$CH_3CH_2CH_2CH_2NH_2 \rightarrow CH_3CH_2CH_2CH_2^* + NH_2^* \quad (1)$$

$$CH_3CH_2CH_2CH_2^* + O_2^* \rightarrow CO_2^* + H_2O^* \quad (2)$$

As shown in Fig. 3, the intensity of the vibration peaks at 1583 and 1555 cm^{-1} increased as the temperature increased from 100 °C to 250 °C. When the temperature increased from 100 °C to 250 °C, some portion of NH_2^* was oxidized into nitrate species (1555 cm^{-1}, monodentate nitrate) and then NH_2^* reacted with surface nitrate species, leading to the production of N_2 and N_2O. Within this temperature range, the formation of N_2 exceeded NO production. Therefore, we inferred that the reaction rate of Eq. 4 is greater than Eq. 3, and the formation of NO* (Eq. 3) is a rate-controlled step (Eqs. 3-6).

$$NH_2^* + O_2^* \rightarrow NO^* + H_2O^* \quad (3)$$

$$NH_2^* + NO^* \rightarrow N_2^* + H_2O^* \quad (4)$$

$$NH_2^* + NO^* \rightarrow N_2O^* + 2H^{+*} + 2e \quad (5)$$

$$NH_2^* + H^{+*} + e \rightarrow NH_3^* \quad (6)$$

At $T > 250$ °C, the gaseous O_2 directly participated in the reaction, and then the NH_2^* was over oxidized into bidentate nitrate species. According to Fig. 3c, monodentate nitrate (1555 cm^{-1}) appeared at temperatures from 100 °C to 250 °C and then was further oxidized to bidentate nitrate species (1569 cm^{-1}) at $T > 250$ °C. Hence, we speculated that the reaction rate of Eq. 7 was higher than Eq. 8, most of NH_2^* was oxidized to stable nitrate species, and the concentration of NH_2^* was not sufficient for NO* reduction. At this time, the rate-controlled step was the formation of N_2^* (Eq. 8). Moreover, NO_2 was generated through the reaction of NO with O_2 at high temperatures. These processes were described by Eqs. 7–9.

$$NH_2^* + O_2^* \rightarrow NO^* + H_2O^* \quad (7)$$

$$NH_2^* + NO^* \rightarrow N_2^* + H_2O^* \quad (8)$$

$$2NO^* + O_2^* \leftrightarrow 2NO_2^* \quad (9)$$

Theoretical calculations were performed to study the formation energy of oxygen vacancy, the adsorption of reactants and product molecules and the reaction mechanism. In general, oxygen vacancies play a vital role in catalytic oxidation reactions. In the present study, the formation energies of two different oxygen vacancies (labeled as $O_{vCe2Zr1}$ and O_{vCe3}) were calculated for the pure $CeZrO_2(111)$, as shown in Fig. 4a. The optimized geometry of the structures of $CeZrO_2(111)$ with $O_{vCe2Zr1}$ and O_{vCe3} vacancies are presented in Figs. 4b and c, respectively. The calculated formation energy for $O_{vCe2Zr1}$ and O_{vCe3} vacancies are 3.10 and 4.08 eV, respectively, indicating that the formation of O vacancy on pure $CeZrO_2$ has certain difficulties. Moreover, the structure of the Cu-doped $CeZrO_2(111)$ was first investigated and the formation energies of four different oxygen vacancies (labeled as O_{v1}, O_{v2}, O_{v3} and O_{v4}) were calculated, as shown in Fig. 4d. The doping of Cu promoted the formation of oxygen vacancies, as the calculated E_{ov} values near the doped Cu (O_{v1}, O_{v2}, O_{v3} and O_{v4}) are much lower than the formation energy of $O_{vCe2Zr1}$ and O_{vCe3} vacancies. In particular, the calculated E_{ov} value for O_{v1} is negative, indicating that an oxygen vacancy forms spontaneously. Therefore, further computations in this study were performed using the model of a Cu-doped $CeZrO_2(111)$ slab with an O_{v1} vacancy.

The adsorption energies of reactants and products are presented in Fig. S9 (Supporting information). The pure facets of Cu-doped $CeZrO_2(111)$ have a lower binding strength for O_2, and the adsorption energy is very small (–0.01 eV), indicating the very weak physical adsorption of O_2 on this facet. Interestingly, as oxygen vacancies are introduced to the Cu-doped $CeZrO_2(111)$, the adsorption energy of O_2 becomes higher, indicating that an oxygen vacancy is more conducive to the selective catalytic oxidation of *n*-butylamine. O_2 and *n*-butylamine molecules display relatively stronger binding strengths (–0.37 and –0.67 eV, respectively), while N_2 and CO_2 present very weak adsorption strengths (–0.04 and –0.12 eV, respectively). The distinct adsorption strengths will potentially improve the catalytic performance of Cu-doped $CeZrO_2(111)$ in butylamine oxidation, as the reactant easily adsorbs, while the products will desorb rapidly.

The minimum energy pathway for *n*-butylamine oxidation was subsequently calculated to further verify the *n*-butylamine adsorp-

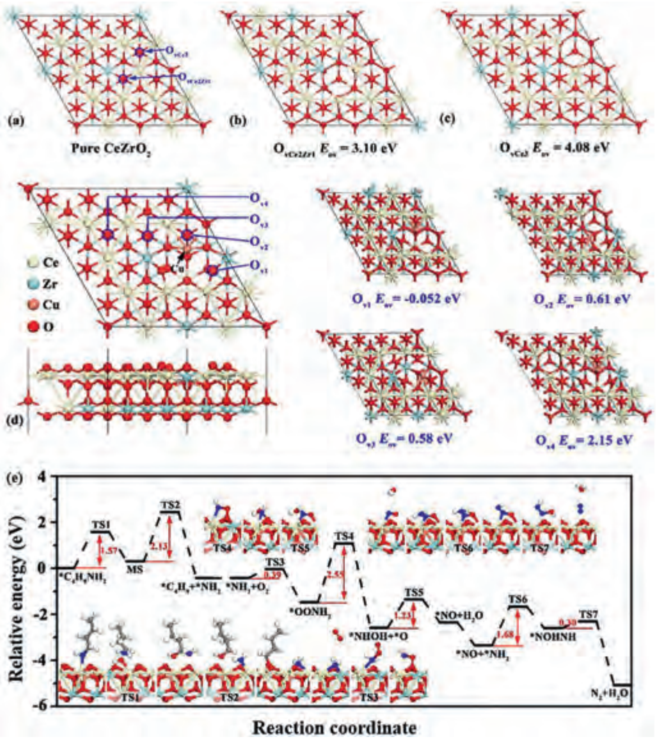

Fig 4. (a) Optimized geometry structures of pure $CeZrO_2(111)$, (b) $CeZrO_2(111)$ with $O_{vCe2Zr1}$, (c) $CeZrO_2(111)$ with O_{vCe3} and the formation energy of oxygen vacancy. (d) Top and side views of the structure of Cu-doped $CeZrO_2(111)$ and the formation energy of oxygen vacancy (O_{v1}, O_{v2}, O_{v3} and O_{v4}). (e) Minimum energy pathway for the dissociation of *n*-butylamine and the oxidation of NH_2 into N_2. Insets are the corresponding structures.

tion on the surface of the catalyst and the formation of intermediate species and N_2 during the reaction. As shown in Fig. 4e, *n*-butylamine in the gas phase was initially adsorbed on exposed Ce atoms near the O_{v1} vacancy to form an adsorbed *n*-butylamine molecule. First, the C–H bond was attacked by a neighboring O to produce MS ($CH_3CH_2CH_2CHOHNH_2$) species; this process should overcome an energy barrier of 1.57 eV. Subsequently, the C–N bond was dissociated into $^*C_4H_9$ and $^*NH_2$ species, which will adsorb on the exposed Ce atom and the neighboring O atom, respectively.

For the selective catalytic oxidation reaction of *n*-butylamine, we mainly focused on the formation of N_2. The transition states and reaction pathways were calculated to further confirm the mechanism of N_2 generation from $^*NH_2$ species, as evidenced by *in situ* DRIFTs. O_2 was adsorbed on oxygen vacancies (O_{v1}) and reacted with $^*NH_2$ species to form $^*OONH_2$ species with an energy of 0.39 eV, indicating that this reaction readily occurred. Subsequently, the O atom of $^*OONH_2$ species was attacked by the H atom of $^*OONH_2$ species, conquering a high energy barrier of 2.55 eV to produce the *NHOH species. Then, the O atom of the *NHOH species was again attacked by the H atom to form the *NO species with an energy barrier of 1.23 eV. At this time, *NO species occupied the position of the original oxygen vacancy (O_{v1}). The $^*NH_2$ species was adsorbed on the *NO species, and should surmount an energy barrier of 1.68 eV to obtain the *NOHNH species. Finally, the H atom of the *NOHNH species attacked the O atom to generate the end product of N_2 after H_2O was stripped.

In short, $^*NH_2$ was oxidized into N_2 through the following steps Eqs. 10 and 11:

$$^*NH_2 + O_2 = {}^*OONH_2 = {}^*NHOH + {}^*O = {}^*NO + H_2O \tag{10}$$

$$^*NO + NH_2 = {}^*NOHNH = N_2 + H_2O \tag{11}$$

The rate-determining step of the whole process is $^*OONH_2 = {}^*NHOH + {}^*O$, with an energy barrier of 2.55 eV. Notably, the energy barriers were calculated without considering the effects of coverage, O_2 pressure, solvent, *etc.* Therefore, the actual reaction barriers would be much lower, indicating that the catalytic oxidation of *n*-butylamine through the proposed pathway may be feasible.

In conclusion, a series of mixed $CeCu_aZrO_x$ oxides were successfully synthesized and tested for *n*-butylamine selective catalytic oxidation. The $CeCu_aZrO_x$ sample with 10% Cu showed excellent performance, exhibited 100% conversion of *n*-butylamine and 90% N_2 selectivity at 250 °C. $CeCu_{10\%}ZrO_x$ displayed the highest redox ability, the reduction peak of the highly dispersed copper oxide species was located at a lower temperature, and the H_2 consumption of this peak is maximum. The incorporation of Cu into $CeZrO_x$ significantly increased the proportion of $Ce^{3+}/(Ce^{3+} + Ce^{4+})$. Additionally, more chemisorbed oxygen species and oxygen vacancies were presented in $CeCu_{10\%}ZrO_x$. The changes in oxygen vacancies over $CeCu_{10\%}ZrO_x$ during reaction process were studied by *in situ* Raman spectra, and the number of oxygen vacancies gradually increased as the temperature increased. Theoretical calculations were performed to study the formation energy of oxygen vacancy, the doping of Cu could promote the formation of oxygen vacancy as the oxygen vacancies formation energy of $CuCeZrO_x$ was much lower than that of pure $CeZrO_x$. Furthermore, the catalytic reaction mechanism underlying *n*-butylamine selective catalytic oxidation was proposed as described below. First, *n*-butylamine and O_2 were adsorbed on the oxygen vacancy (O_{v1}), and then *n*-butylamine was attacked by the neighbor O to produce MS ($CH_3CH_2CH_2CHOHNH_2$) species. Subsequently, the C-N bond was dissociated, forming CH_3-CH_2-CH_2-CH_2^* and NH_2^*. CH_3-CH_2-CH_2-CH_2^* was further oxidized into CO_2 and H_2O, and NH_2^* could be oxidized to NO/nitrate species through important intermediate species ($^*OONH_2$ and *NHOH). Finally, NH_2^* reacted with NO/nitrate species, leading to the production of N_2 and H_2O. The results of the present study are believed to provide a deeper understanding of the catalytic mechanisms and a high-performance removal of NVOCs.

Declaration of competing interest

The authors declare that they have no known competing financial interests or personal relationships that could have appeared to influence the work reported in this paper.

Acknowledgments

This work is financially supported by the R&D Program of Beijing Municipal Education Commission (No. KJZD20191443001), Beijing Municipal Science and Technology Commission (No. Z181100000118003), the Fundamental Research Funds for the Central Universities and Doctoral Research Start-up Fund Project of Taiyuan University of Science and Technology (No. 20202053).

Supplementary materials

Supplementary material associated with this article can be found, in the online version, at doi:10.1016/j.cclet.2021.09.056.

References

[1] C. He, J. Cheng, X. Zhang, et al., Chem. Rev. 119 (2019) 4471–4568.
[2] L.F. Liotta, Appl. Catal. B: Environ. 100 (2010) 403–412.
[3] J. Yang, Y. Guo, Chin. Chem. Lett. 29 (2018) 252–260.
[4] M. Wang, M. Shao, S. Lu, Y. Yang, W. Chen, Chin. Chem. Lett. 24 (2013) 829–832.
[5] G. Wang, Z. Zhang, Z.P. Hao, Crit. Rev. Environ. Sci. Technol. 49 (2019) 2257–2313.

[6] H. Chen, Y. Yang, Q. Liu, et al., RSC Adv. 9 (2019) 8454–8462.
[7] T. Nanba, S. Masukawa, J. Uchisawa, A. Obuchi, Catal. Lett. 93 (2004) 195–201.
[8] T. Nanba, S. Masukawa, A. Ogata, J. Uchisawa, A. Obuchi, Appl. Catal. B: Environ. 61 (2005) 288–296.
[9] T. Nanba, S. Masukawa, A. Ogata, J. Uchisawa, A. Obuchi, J. Mol. Catal. A: Chem. 276 (2007) 130–136.
[10] R. Zhang, D. Shi, N. Liu, Y. Cao, B. Chen, Appl. Catal. B: Environ. 146 (2014) 79–93.
[11] Q. Huang, S. Zuo, R. Zhou, Appl. Catal. B: Environ. 95 (2010) 327–334.
[12] M. Ma, H. Huang, C. Chen, et al., Mol. Catal. 455 (2018) 192–203.
[13] J. Paier, C. Penschke, J. Sauer, Chem. Rev. 113 (2013) 3949–3985.
[14] Z. Ma, D. Weng, X. Wu, Z. Si, J. Environ. Sci. 24 (2012) 1305–1316.
[15] D. Zhang, X. Du, L. Shi, R. Gao, Dalton Trans. 41 (2012) 14455–14475.
[16] Z. Wang, Z. Qu, X. Quan, et al., Appl. Catal. B: Environ. 134-135 (2013) 153–166.
[17] Z. Si, D. Weng, X. Wu, J. Yang, B. Wang, Catal. Commun. 11 (2010) 1045–1048.
[18] P. Li, Y. Xin, Q. Li, et al., Environ. Sci. Technol. 46 (2012) 9600–9605.
[19] S. Ding, F. Liu, X. Shi, et al., ACS Appl. Mater. Interfaces 7 (2015) 9497–9506.
[20] S. Ding, F. Liu, X. Shi, H. He, Appl. Catal. B: Environ. 180 (2016) 766–774.
[21] X. Zhang, G. Dou, Z. Wang, et al., Catal. Sci. Technol. 3 (2013) 2778–2785.
[22] J. Zhu, Z. Zhao, D. Xiao, et al., J. Mol. Catal. A: Chem. 238 (2005) 35–40.
[23] L. Liu, Z. Yao, B. Liu, L. Dong, J. Catal. 275 (2010) 45–60.
[24] R. Si, Y. Zhang, S. Li, B. Lin, C. Yan, J. Phys. Chem. B 108 (2004) 12481–12488.
[25] G. Postole, B. Chowdhury, B. Karmakar, et al., J. Catal. 269 (2010) 110–121.
[26] X. Du, D. Zhang, L. Shi, R. Gao, J. Zhang, J. Phys. Chem. C 116 (2012) 10009–10016.
[27] X. Wang, Y. Pan, H. Ning, et al., Appl. Catal. B: Environ. 266 (2020) 118630.
[28] S. Wang, T. Zhang, Y. Su, et al., Catal. Lett. 121 (2007) 70–76.
[29] Z. Wang, X. Sun, J. Liu, X. Li, Surf. Interfaces 6 (2017) 103–109.
[30] W. Shan, W. Shen, C. Li, Chem. Mater. 15 (2003) 4761–4767.
[31] D. Gamarra, G. Munuera, A.B. Hungria, et al., J. Phys. Chem. C 111 (2007) 11026–11038.
[32] H. He, X. Lin, S. Li, et al., Appl. Catal. B: Environ. 223 (2018) 134–142.
[33] J. Xu, P. Li, X. Song, et al., J. Phys. Chem. Lett. 1 (2010) 1648–1654.
[34] Y. Lee, G. He, A.J. Akey, et al., J. Am. Chem. Soc. 133 (2011) 12952–13955.
[35] X. Lin, S. Li, H. He, et al., Appl. Catal. B: Environ. 223 (2018) 91–102.
[36] H. Praliaud, S. Mikhailenko, Z. Chajar, M. Primet, Appl. Catal. B: Environ. 16 (1998) 359–374.
[37] P. Ratnasamy, D. Srinivas, C.V.V. Satyanarayana, et al., J. Catal. 221 (2004) 455–465.
[38] J.P. Espinós, J. Morales, A. Barranco, et al., J. Phys. Chem. B 106 (2002) 6921–6929.
[39] Q. Wang, H. Xu, W. Huang, Z. Pan, H. Zhou, J. Hazard. Mater. 364 (2019) 499–508.
[40] N. Guillén-Hurtado, A. Bueno-López, A. García-García, J. Mater. Sci. 47 (2011) 3204–3213.
[41] A. Łamacz, A. Krztoń, G. Djéga-Mariadassou, Catal. Today 176 (2011) 126–130.
[42] E. Moretti, L. Storaro, A. Talon, et al., Microporous Mesoporous Mater. 116 (2008) 575–580.
[43] G. Ramis, G. Busca, J. Mol. Struct. 193 (1989) 93–100.
[44] N. Oktar, J. Mitome, E.M. Holmgreen, U.S. Ozkan, J. Mol. Catal. A: Chem. 259 (2006) 171–182.
[45] L. Zhang, H. He, J. Catal. 268 (2009) 18–25.
[46] R. Zhang, P. Li, R. Xiao, N. Liu, B. Chen, Appl. Catal. B: Environ. 196 (2016) 142–154.
[47] Z. Zhang, Y. Zhang, Q. Su, et al., Environ. Sci. Technol. 44 (2010) 8254–8258.
[48] R. Guo, X. Sun, J. Liu, et al., Appl. Catal. A: Gen. 558 (2018) 1–8.